PNAS RESEARCH ARTICLE | SUSTAINABILITY SCIENCE

A polyimine aerogel separator with electron cloud design to boost Li-ion transport for stable Li metal batteries

Luoyi Ding[a,1], Xinyang Yue[a,1], Xinhai Zhang[a,2], Yuanmao Chen[a], Jijiang Liu[a], Zhangqin Shi[a], Zhiyong Wang[a], Xuzhou Yan[a,2], and Zheng Liang[a,2]

Edited by Alexis Bell, University of California, Berkeley, CA; received August 18, 2023; accepted November 7, 2023

The separator with high Young's modulus can avoid the danger of large-sized dendrites, but regulating the chemical behavior of lithium (Li) at the separator/anode interface can effectively eliminate the dendrite issue. Herein, a polyimine aerogel (PIA) with accurate nitrogen (N) functional design is used as the functional separator in Li metal batteries to promote uniform Li nucleation and suppress the dendrite growth. Specifically, the imine (N1) and protonated tertiary amine (N2) sites in the molecular structure of the PIA are significantly different in electron cloud density (ECD) distribution. The N1 site with higher ECD and the N2 site with lower ECD tend to attract and repulse Li^+ through electrostatic interactions, respectively. This synergy effect of the PIA separator accelerates the interfacial Li^+ diffusion on the Li anode to sustain a uniform two-dimensional Li nucleation behavior. Meanwhile, the well-defined nanochannels of the PIA separator show high affinity to electrolyte and bring uniform Li^+ flux for Li plating/stripping. Consequently, the dendrites are effectively suppressed by the PIA separator in routine carbonate electrolyte, and the Li metal batteries with the PIA separator exhibit high Coulombic efficiency and stable high-rate cycling. These findings demonstrate that the ingenious marriage of special chemical structure designs and hierarchical pores can enable the separator to affect the interfacial Li nucleation behavior.

polyimine aerogel | covalent polymer network | Li metal battery | Li-ion diffusion | separator engineering

Significance

Porous materials have been widely applied to address Li dendrite-related problems, especially in the field of separator engineering, due to their distinctive advantages of high porosity, adjustable pore structures, and easy functionalization. However, developing functional integrated and self-supporting separators through ingenious molecular-level structural design has been rarely explored thus far. Herein, a self-supporting PIA separator containing rich hierarchical pores and polar skeleton was fabricated to regulate the interfacial Li chemical behavior for restricting the dendrite growth of Li metal. This work provides a favorable separator design approach suggested for the performance enhancement of LMBs.

Lithium metal batteries (LMBs) have attracted intensive attention owing to their high theoretical specific capacity (3,860 mAh g^{-1}) and the lowest negative electrochemical reduction potential (–3.04 V vs. the standard hydrogen electrode) (1–3). Unfortunately, the performance of LMBs always suffers from the formation of lithium (Li) dendrites during the repeated Li plating/stripping process because of the unstable anode/electrolyte interface. The uncontrollable dendrite growth causes many issues, such as limited Coulombic efficiency (CE), dissatisfied cycling stability, and dendrite-induced safety hazards, which are the bottleneck to the LMB's real-world services (4–6).

The separator, as one of the crucial components of LMBs, not only accommodates the electrolyte and separates the electrodes but also has a nonnegligible impact on the chemical behavior of the Li^+ on the anode interface (7). Although polyolefin separators such as polypropylene (PP) and polyethylene (PE) have been widely used in LMBs due to their outstanding chemical and electrochemical parameters, separator modifications are oftentimes adopted to tame the Li metal. Typically, the functional coating used for separator modification mainly includes polymer-based materials [poly(pentafluorophenyl acrylate) (8), polyacrylate acid (9)], ceramic compounds [SiO_2 (10), Al_2O_3 (11), and $Li_{6.75}La_3Zr_{1.75}Ta_{0.25}O_{12}$ (12)], metal [Mg (13), Bi (14)] and metal composites [MgF_2 (15), $MnCO_3$ (16)], and carbon-based materials [graphene oxide (17), graphene (18)]. Based on these, the interfacial issue of Li metal can be largely resolved, particularly in the inhibition of Li dendrite. Nevertheless, the coating may fall off the separator under the stress fluctuations derived from Li deposition, resulting in modification failure. Besides, the functional coating materials will cause unnecessary hazard reactions with the electrolyte and even block the pores of the separator to hinder the Li^+ transfer (19, 20). Therefore, it seems to be particularly considerable to develop a class of functional integrated and self-supporting separators to meet the requirements of LMBs.

In recent years, porous materials have been widely applied to address Li dendrite-related problems, especially in the field of separator engineering, because of their distinctive properties such as high porosity, large specific surface, adjustable pore structures, and easy functionalization. The research hotspots of porous materials mainly focus on covalent-organic frameworks (COFs) (21), metal-organic frameworks (MOFs) (22), zeolites (23) as well as aerogels (24). In addition to the porous merits of these materials, more ingenious molecular-level structures in separator engineering need to be established, to inhibit the formation of dendrites by affecting the initial Li nucleation. That is to say, the interaction

Author affiliations: [a]Frontiers Science Center for Transformative Molecules, School of Chemistry and Chemical Engineering, Shanghai Jiao Tong University, Shanghai 200240, People's Republic of China

Author contributions: X.Z., X. Yan, and Z.L. designed research; L.D. and X.Z. performed research; Y.C., J.L., Z.S., and Z.W. contributed new reagents/analytic tools; L.D., X. Yue, X.Z., Y.C., J.L., Z.S., Z.W., X. Yan, and Z.L. analyzed data; and L.D., X. Yue, and X.Z. wrote the paper.

The authors declare no competing interest.

This article is a PNAS Direct Submission.

[1]L.D. and X. Yue contributed equally to this work.

[2]To whom correspondence may be addressed. Email: xhzhang06@sjtu.edu.cn, xzyan@sjtu.edu.cn, or liangzheng06@sjtu.edu.cn.

This article contains supporting information online at https://www.pnas.org/lookup/suppl/doi:10.1073/pnas.2314264120/-/DCSupplemental.

Published December 15, 2023.

between the Li^+ and separator on the anode interface should be valued and utilized in the LMBs community. However, the development of such functional integrated and self-supporting separators has been rarely explored thus far.

In this work, a self-supporting polyimine aerogel (PIA) separator was fabricated via the ingenious bottom–up chemical structural design. In specific, a tris(2-aminoethyl)amine (TREN) featured by a tertiary amine reacted with 1,3,5-tris(p-formylphenyl)benzene (TFPB) through aldimine condensation to construct a PIA's network structure. Therefore, the PIA contains abundant imine (C=N) and tertiary amine. Because of the differences in electron cloud density (ECD) distribution, under electrostatic interaction, the C=N (N1) and protonated tertiary amine (N2) sites could attract and repulse Li^+ diffusing on Li metal surface, respectively. According to the theory analysis, the N1–N2 synergy of the PIA separator can effectively accelerate the Li^+ diffusion within the PIA/Li metal interface, thus suppressing the formation of local current density and facilitating the uniform two-dimensional Li nucleation and dendrite-free deposition. In addition, the abundant hierarchical pore structures of the PIA separator are beneficial to the high ionic conductivity and abundant Li^+ flux. In a routine carbonate electrolyte (RCE), the CE of the PIA-based cell was more than twice that of the cell using the PP separator, and no obvious Li dendrites were observed. The PIA separator was also assembled into the LMBs containing $LiFePO_4$ or high-voltage $LiNi_{0.8}Co_{0.1}Mn_{0.1}O_2$ cathode, showing competitive performance.

Results

Illustration of the PIA Separator in Regulating Li Deposition. Many factors influence Li nucleation, such as interfacial energy, critical nucleation radius, and interfacial diffusion barrier of ions. Therefore, poor separator/anode contact interface and the lack of interface regulation ability of conventional separators likely induce the formation of dendrites (Fig. 1*B*). We propose a de novo design for a self-supporting PIA separator. Typically, the mixture of TREN and TFPB was spread on the Teflon film to gelate. After solvent exchange and supercritical drying, a self-supporting PIA was obtained (Fig. 1*A*). The PIA not only has abundant hierarchical porous structures but also is rich in C=N and tertiary amine. The N atom of the C=N bond is in a state of sp^2 hybridization, where the lone-pair electrons are located in the *s* orbital of the N atom. For tertiary amine, its sp^3 hybridized N atom is connected to three electron-rich methylene groups. Theoretically, tertiary amine is more prone to protonation by binding with hydrogen ions in the electrolyte, and then the protonated tertiary amine group shows lower ECD relative to that of the C=N. As a result, the C=N (N1) with higher ECD and protonated tertiary amine (N2) with lower ECD tend to attract and repulse Li^+ through electrostatic interactions, respectively. We speculated that this synergistic effect of PIA induced by diverse ECD distribution could accelerate Li^+ diffusion at the Li metal interface to reduce the Li nucleation barrier and suppress the formation of local current density, ensuring a uniform Li deposition (Fig. 1*C*).

Physicochemical Properties Analysis of PIA Separator. The synthesis procedure of the PIA separator is summarized in Supporting Information (*SI Appendix*, Scheme S1) and the formation of TFPB is supported by the proton magnetic resonance (^{1}H NMR) (*SI Appendix*, Fig. S1). With the TFPB in hand, the PIA separator was subsequently constructed by simple one-step condensation polymerization combined with sequential solvent and supercritical drying. In the Fourier transform infrared spectroscopy (FT-IR) spectrum (Fig. 2*A*), the peak at 1,639 cm^{-1} belonging to the C=N bond is highlighted while the peak at 1,684 cm^{-1} allocated to the C=O stretching vibration vanished, suggestive of the completion

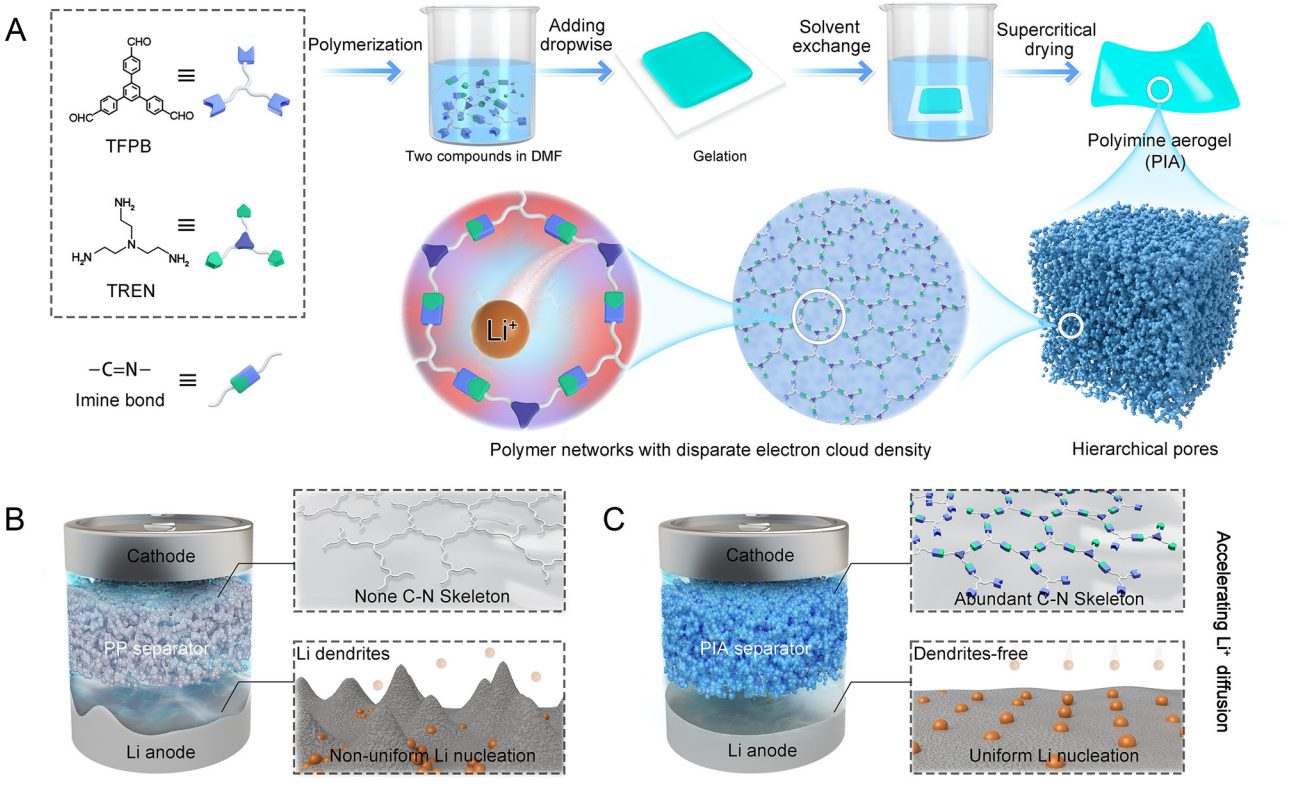

Fig. 1. Schematic of the PIA separator fabrication and the capability of the PIA separator in regulating Li deposition. (*A*) Illustration of the PIA separator fabrication progress. The interfacial Li^+ diffusion and Li nucleation on the Li metal in (*B*) PP and (*C*) PIA separator systems.

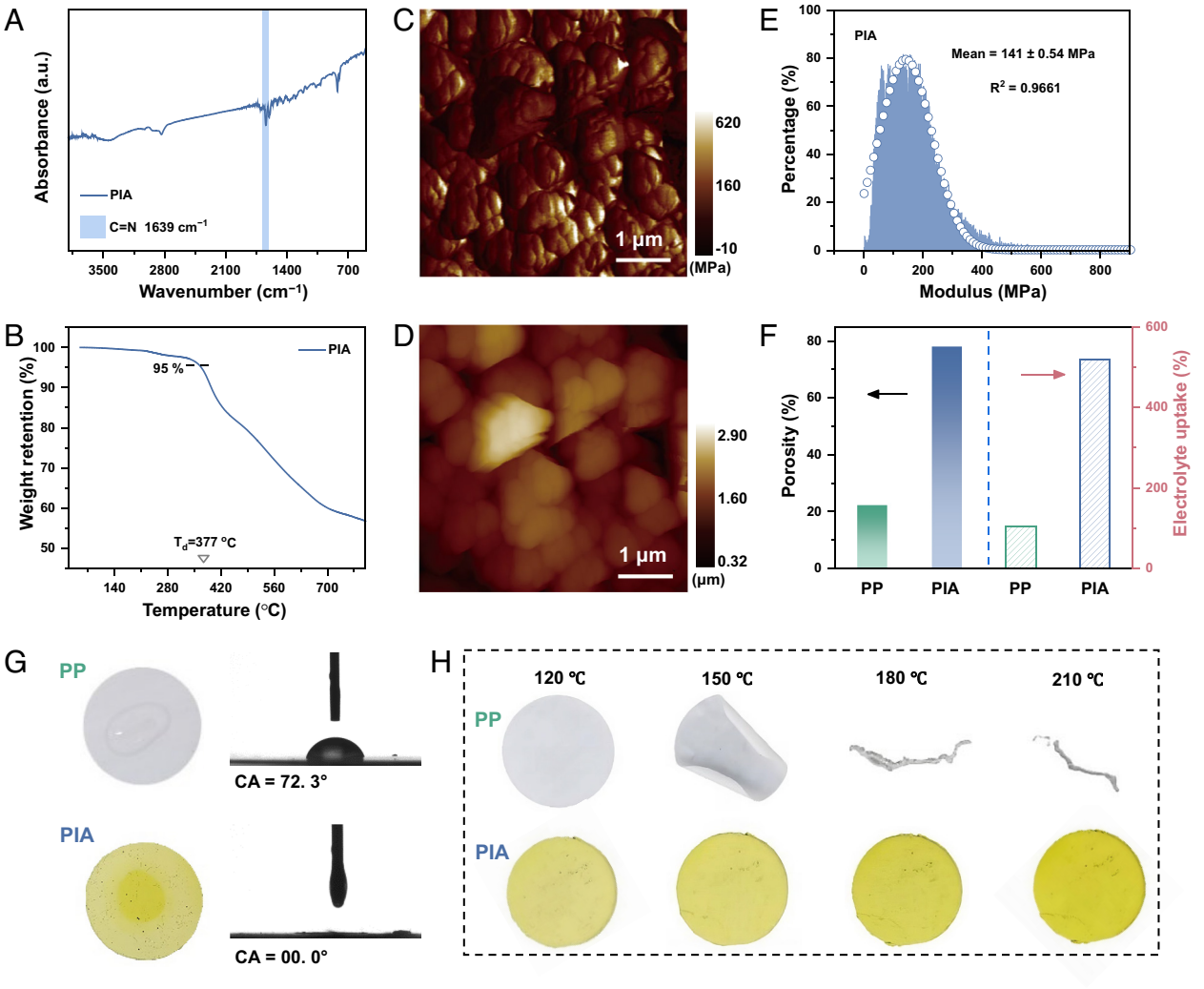

Fig. 2. Physicochemical properties of PIA separator. (*A*) FT-IR curves of the PIA separator. (*B*) TGA profiles of the PIA separator were recorded under N_2 flow with a heating rate of 10 °C min^{-1}. (*C*) AFM height image of the PIA separator. (*D*) Modulus distribution and (*E*) the Young's modulus of the PIA separator obtained from the AFM modulus distribution profiles. (*F*) The porosity and electrolyte uptakes of the PP and PIA separators. (*G*) Electrolyte wettability and the corresponding contact angles of PP and PIA separators. (*H*) Digital images of the PP and PIA separators after heat treatment for 10 min at different temperatures.

of condensation polymerization between TFPB and TREN. (*SI Appendix,* Fig. S2) (25). In addition, the thermogravimetry analysis (TGA) shows the PIA has higher thermal stability than that of the PP (Fig. 2*B* and *SI Appendix,* Fig. S3). When the thermal destruction temperature exceeds 377 °C, only 5% weight loss takes place. Noticeably, the scanning electron microscope (SEM) discloses uniform and abundant nano-micro pores in the PIA separator (*SI Appendix,* Fig. S4), which is conducive to the diffusion of the ions in electrolytes (26). The thickness of the free PIA separator was determined to be ~50 μm, which was also acceptable (*SI Appendix,* Fig. S5). In addition, atomic force microscopy (AFM) height images of the PIA separator further verified the porous structures (Fig. 2*C*). Despite that high porosity deprave the strength of almost all materials, the PIA separator exhibits excellent mechanical property and relatively uniform modulus distribution based on the AFM modulus distribution profiles (Fig. 2 *D* and *E*), which implies that the robust PIA separator has the potential to resist the attack by large-sized dendrites (27).

Importantly, there are still abundant hierarchical pores in the PIA even being squeezed (*SI Appendix*, Figs. S4 *A* and *B* and S6). The element distribution contour of the squeezed PIA corresponds to the morphology (*SI Appendix,* Fig. S4 *C–F*), which indicates the high structural stability of the skeleton and pores of PIA. The electrolyte uptake and porosities of the PIA separator are much higher than that of PP (electrolyte uptake: 591% vs. 104%, porosities: 78% vs. 23%) (Fig. 2*F*). The contact angle test also verified the improved electrolyte wettability of PIA separator (Fig. 2*G*). It is demonstrated that the PIA separator can maintain a high Li^+ conductivity and uniform Li^+ flux. For another, the thermostability test revealed that the PIA separator can keep stability above 210 °C (Fig. 2*H*), which coincides with the results of TGA. This feature would contribute to the battery operation under elevated temperatures and prevent the occurrences of safety hazards (28). By comparison, the PP separator shrinks and gradually melts when the temperature rises to 150 °C.

Characteristic of Li^+ Transport in PIA Separator. The ionic conductivity of the electrolyte-infiltrated separators was collected by the electrochemical impedance spectroscopy (EIS) spectra of the symmetric cells using stainless steel (SS) (*SI Appendix,* Fig. S7) (29). The PP-based cell exhibits an ionic conductivity of ~0.23 mS cm^{-1}, whereas a sharp contrast is found in the PIA sample, presenting a higher ionic conductivity (0.92 mS cm^{-1}) (Fig. 3*A*). Subsequently, the values of Li^+ transference number (t_{Li}^+) in different systems were further calculated, as shown in

SI Appendix, Fig. S8. The t_{Li}^+ of electrolyte in PIA and PP is 0.78 and 0.39, respectively, which is due to the obstruction of the diffusion/migration of anions having large molecular volume by the abundant and well-defined nanochannels of PIA. In this case, the formation of space charge on the PIA/Li metal interface will be restrained during Li plating, which reduces the tendency for uneven dendrite growth. Moreover, the PIA separator performs high electrochemical stability because the free volume and pores of the molecular chains become smaller induced by the π–π stacking of benzene rings in the cross-linked network. As Fig. 3*B* shows, the PIA can withstand the 4.5 V (vs. Li/Li^+) oxidation potential, whereas an obvious increase in anodic current can be detected in the cell using a PP separator when the potential reaches 4.1 V (vs. Li/Li^+). Therefore, the PIA separator has the intrinsic advantage of working in high-voltage LMBs with RCE (30).

According to the Tafel plot (Fig. 3*C* and *SI Appendix,* Fig. S9), the exchange current density (j_0) of PIA-based Li symmetric cell is 0.64 mA cm^{-2}, higher than that of PP-based cells (0.33 mA cm^{-2}), indicating an enhanced charge-exchange behavior at the PIA/Li metal interface (31). The reason for this difference in reaction kinetics is possibly due to the following reasons: 1) the Li desolvation process becomes easier when the anion is confined by the PIA separator; 2) the lower diffusion barrier of Li^+ on the PIA/Li metal interface facilitates the initial Li nucleation. Noted that apart from the confinement effect of nanochannels of PIA, the C=N bonds in PIA configuration are also able to weaken the interaction between the Li^+ and the solvent molecules to promote the Li^+ desolvation process (32). The energy barriers of the Li^+ desolvation energy have an obvious change in different systems. (*SI Appendix,* Figs. S10 and S11). Cyclic voltammetry (CV) measurement of $LiFePO_4$ (LFP)||Li metal full-cells were conducted to estimate the Li^+ diffusion coefficient (D_{Li}^+). Based on the Randles–Sevcik equation (33), the PIA-based cell shows a higher D_{Li}^+ (2.41×10^{-10} cm^2 S^{-1}) compared to that of the PP-based cell (1.37×10^{-10} cm^2 S^{-1}) (Fig. 3*D*). However, the Li^+ diffusion in cell system includes two parts: bulk phase diffusion and interfacial diffusion. Therefore, whether PIA can accelerate interfacial diffusion still needs to be explored by more in-depth theoretical analysis.

Theoretical Analyses of the Electron Cloud Synergy Induced by PIA Separator. The theoretical analyses were implemented to reveal the reasons behind those remarkable improvements in electrochemical performances for the PIA separator. The chemical structure model of PIA was constructed for the subsequent calculation. There are three reduplicative structural units in the PIA structure model, thus one is chosen to perform the following calculation for optimization understanding (Fig. 4*A*). The electrostatic potential (ESP) which is often used to conjecture the functional sites in organic chemistry was performed to analyze the electrostatic interaction between PIA separator and Li^+ (34). As shown in Fig. 4*B*, the N1 site displayed by the red region belongs to negatively charged as a result of the unsaturated π bond and the lone pairs of the N atom. By contrast, the region of the N2 site shows blue, so the N2 site is positively charged compared to the N1 site. This result coincides well with the analysis of the ECD distribution on the N1 and N2 sites.

Binding energy and charge density analyses were conducted based on DFT calculations for verifying the interactions between the Li and different N-sites (Fig. 4*C* and *SI Appendix,* Figs. S12 and S13) (35). The N atoms belonging to N1 sites (high ECD) and N2 sites (low ECD) exhibit the opposite adsorption energy of –0.65 and +0.28 eV, respectively. It indicates the disparate interaction between Li and N atoms. The N1 sites are expected to attract Li^+ through electrostatic interactions, while the N2 sites are contrary. Therefore, a unique N1–N2 synergy, i.e., a push–pull effect on Li-ions by PIA, will inevitably affect the diffusion

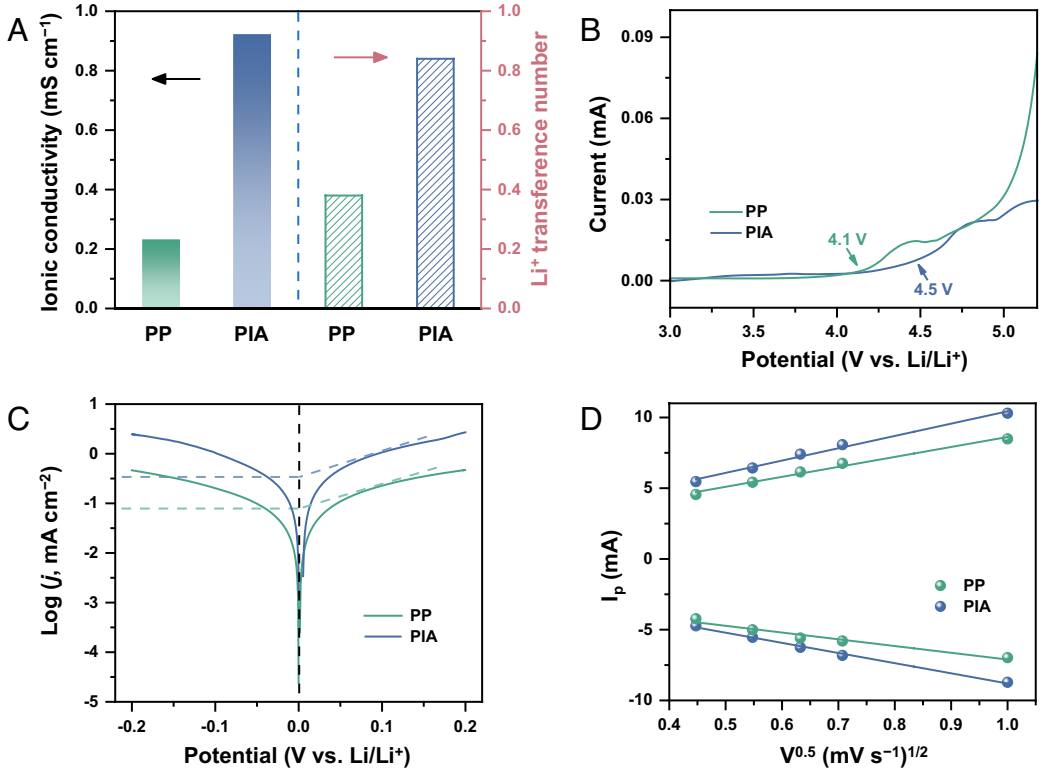

Fig. 3. Li^+ transport in PIA separator. (*A*) The quantitative value of Li^+ conductivity and t_{Li}^+ of PP and PIA separators. (*B*) LSV curves of stainless steel (SS)/separators/Li cells with different separators. (*C*) The Tafel profiles of PP and PIA separators in Li symmetric cells. (*D*) Cathodic and anodic peak currents (I_p) vs. the square root of the scan rate ($v^{0.5}$) for PP and PIA separators.

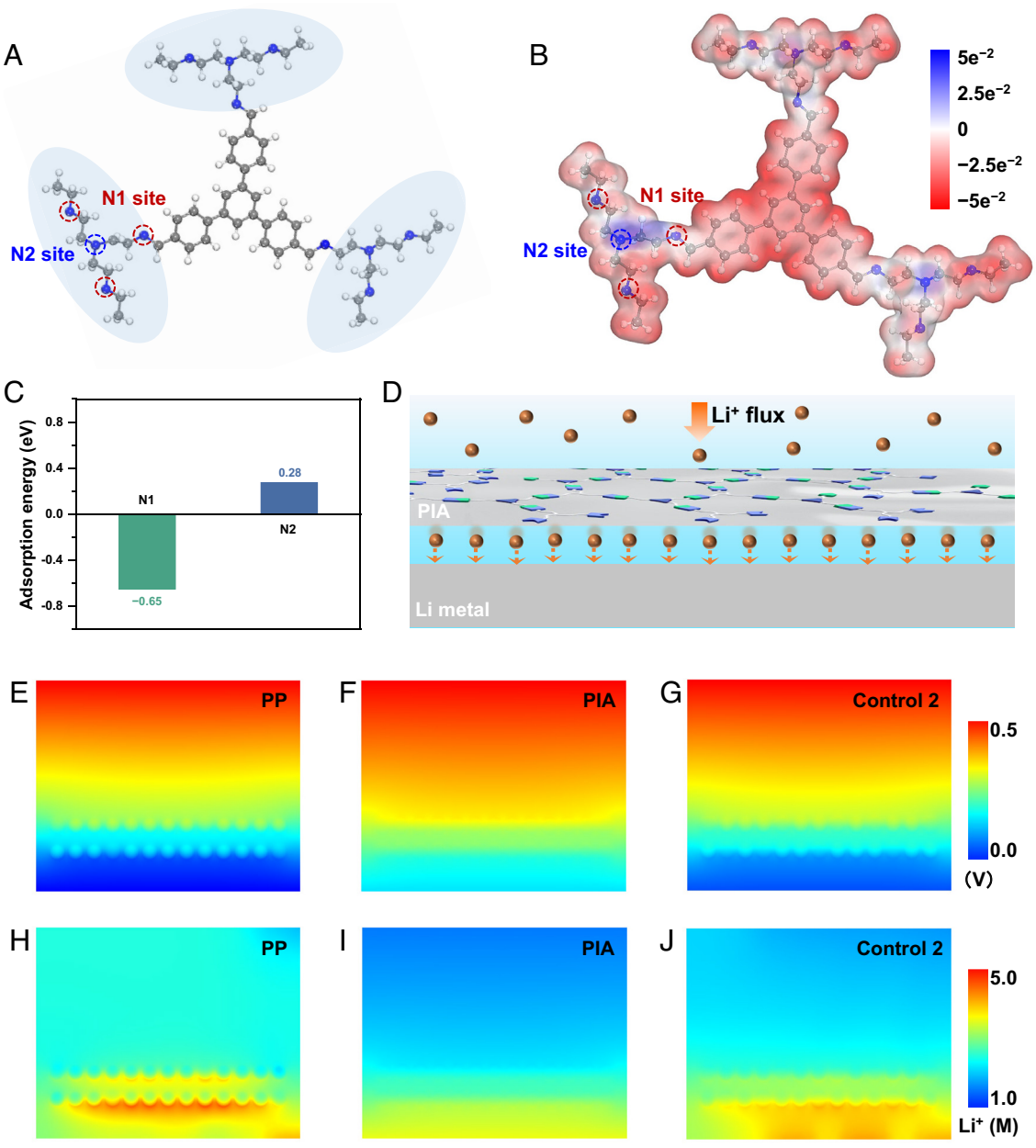

Fig. 4. The electron cloud synergy induced by the PIA separator. (*A*) The chemical structure model of PIA [the one reduplicative structural unit is chosen to label the different N sites (N1 site and N2 site)]. (*B*) Density functional theory (DFT)-calculated electrostatic potential (ESP) of the PIA chemical structure. (*C*) Adsorption energy of a Li atom with N1 site and N2 site in PIA structure model. (*D*) Schematic illustration of Li^+ diffusion at the separator/anode interface. Numerical simulation of the potential distribution at (*E*) PP, (*F*) PIA separator, and (*G*) control 2 (only containing electron-rich N1 sites). The ion concentration distribution at (*H*) PP, (*I*) PIA separator, and (*J*) control 2.

behavior of Li^+ after adsorption on the Li anode surface, thereby affecting the subsequent Li nucleation/deposition (Fig. 4*D*). To note that, the N atoms of PIA separator cannot react with plated Li atoms to form Li_3N because of the smaller electrons transfer between them, which means that the PIA separator possesses high electrochemical stability in working batteries (*SI Appendix,* Fig. S14) (36).

The simulation was carried out with the COMSOL Multiphysics package to detect the interfacial electric field and Li^+ concentration distribution in different systems. For PP-based cell, the uneven surface of the bare Li metal and the large diffusion barrier of Li^+ on Li metal surface will lead to an inhomogeneous interfacial electric field during Li deposition (Fig. 4*E*). The dull Li^+ on PP/Li metal interface not only increases the critical Li nucleation radius and reduces the Li nucleation rates but also promotes the formation of local space charge (37). As Fig. 4*H* and *SI Appendix,* Fig. S15 display, the phenomenon of local current density near the reacting interface is gradually serious as Li deposition proceeds, which tends to cause continuous dendrite growth (38). As shown in *SI Appendix,* Fig. S16 *A–C*, the scattered large Li nucleation deposits are observed, and those nucleation deposits are finally grown into Li dendrites with subsequent continuous deposition.

By contrast, due to the N1–N2 synergy in the PIA separator, the electric field difference on the Li metal surface is distinctly mitigated (Fig. 4*F*). Therefore, such raw electron field brought by PIA can encourage the interfacial Li diffusion to reduce the Li nucleation barrier and promote the uniform Li nucleation. As confirmed in *SI Appendix,* Fig. S17, the nucleation overpotential for the cell using PIA and PP separator is 0.34 and 0.90 V (vs. Li^+/Li), respectively. Moreover, the PIA/Li metal interface reveals a uniform Li^+ flux after

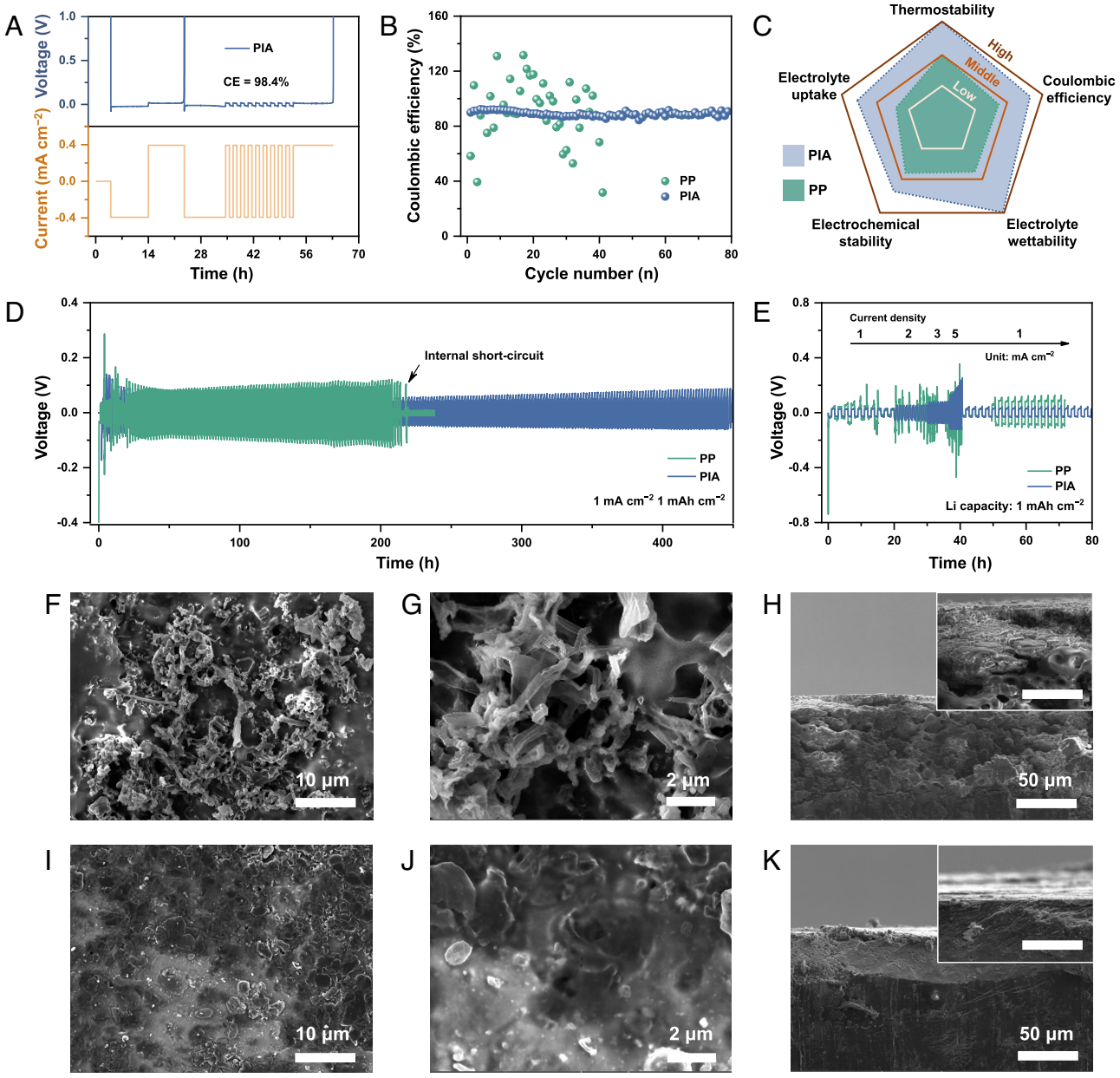

Fig. 5. Electrochemical performance of the Li symmetric cells. (*A*) Voltage-time profiles of Li||Cu half-cell with PIA separator at 0.5 mA cm^{-2}. (*B*) Cycling performance of the Li||Cu half-cells with different separators at 0.5 mA cm^{-2} with 0.5 mAh cm^{-2}. (*C*) A radar chart that compares the related parameters of the PIA separator with those of PP. (*D*) Cycling performance of Li symmetric cells with different separators at 1.0 mA cm^{-2} with 1.0 mAh cm^{-2}. (*E*) Rate performance of the Li symmetric cells at various rates (1.0 to 5.0 mA cm^{-2}) with a fixed 1 mAh cm^{-2}. (*F* and *G*) Surface and (*H*) cross-sectional SEM images of the Li deposition in the cell with PP separator (*Inset* is the high magnification image and the Scale bar is 10 μm). (*I* and *J*) Surface and (*K*) cross-sectional SEM images of the Li deposition in the cell with PIA separator (*Inset* is the high magnification image and the Scale bar is 10 μm).

reaching a steady state (Fig. 4*I* and *SI Appendix,* Fig. S18), where the local current density is significantly suppressed. *SI Appendix,* Fig. S16*D* is the SEM image of the Li deposition under the PIA separator, which shows that the Li crystal nuclei with smaller sizes have a uniform distribution onto Cu foil during the initial nucleation process. As a result, a flat and dense Li deposition morphology without a dendrite format can be achieved by a PIA separator (*SI Appendix,* Fig. S16 *E* and *F*). To determine the Li nucleation model in PP and PIA-based cells, the potentiostatic method was employed. As proved by the potentiostatic measurement (*SI Appendix,* Fig. S19), the calculated Li nucleation model on Li metal anode follows a two-dimensional progressive/instantaneous (2DP/2DI) mode in PIA-based cells (39).

A separator with structures similar to PIA but lacking N2 sites was also analyzed and denoted as control 2. The result demonstrated that the difference in electric field distribution on the control 2/Li metal interface was reduced but still more obvious than that of the PIA system (Fig. 4*G*). Simultaneously, the local current density yielded on reacting interface echoes to the raw interfacial electric field (Fig. 4*J* and *SI Appendix,* Fig. S20). This may be expected because the attractiveness of N1 to Li^+ will also limit the Li^+ diffusion to a certain extent. Since the N2 sites have a chance to promote the desorption of Li^+ near the N1 sites, the existence of N1–N2 synergy in the PIA separator can effectively accelerate the interfacial Li^+ diffusion (*SI Appendix*, Figs. S21–S23). In addition, a separator with structures similar to PIA but lacking N1 sites was also analyzed and denoted as control 3. Correspondingly, there is still a local current density yielded on the reacting interface, which further indicates the advantage of N1–N2 synergy in the PIA separator (*SI Appendix*, Figs. S24 and S25).

Electrochemical Performance Evaluation of the Li Symmetric Cells. To investigate the reversibility of Li plating/stripping behavior, the CEs of the Li||Cu half-cells with different separators were measured using the Aurbach method (40). In Fig. 5*A* and *SI Appendix,* Fig. S26, the average CE of the PIA-based cell (98.4%) is higher than that of the PP-based cell (87.6%), and the polarization of the PIA-based cell is relatively reduced as well. In addition, the stable cycling described in Fig. 5*B* also indicates the significant improvement of the Li plating/stripping reversibility by the PIA separator, in which the PIA-based cell delivered 91% of CE after 80 cycles. This result is highly competitive on account of the excellent comprehensive performance of the PIA separator than that of the PP separator (Fig. 5*C*).

The cycling performance of the Li symmetric cells was performed in Fig. 5*D*. The PIA-based cell exhibited a stable cycling performance (450 h) and lower polarization under 1 mA cm^{-2} with a Li plating capacity of 1 mAh cm^{-2}. However, the cell with the PP separator short-circuited after 218 h of cycling since the separator had been pierced by the large-sized dendrites (*SI Appendix,* Fig. S27). Similarly, at 3.0 mA cm^{-2} and 1.0 mAh cm^{-2}, the PIA-based cell provides lower polarization and improved lifespans than that of the PP-based cell (*SI Appendix,* Fig. S28). The rate performance was conducted at a fixed capacity (Fig. 5*E*). Due to the low interfacial resistance, the PIA-based cell shows steady polarization of 29.5, 54.6, 78.2, 120.1, and 31.3 mV at 1, 2, 3, 5, and 1 mA cm^{-2}, respectively (*SI Appendix,* Fig. S29). In sharp contrast, the PP-based cell reveals higher overpotential and unstable cycles since the dendrite growth and dead Li formation.

After cycles, the Li metal anodes were carefully peeled off from the separator and washed with dimethyl carbonate three times to prepare SEM samples (*SI Appendix,* Fig. S30). For the anode cycled with a PP separator, the SEM image shows porous and loose structures (Fig. 5*F*), and numerous Li dendrites and rod-like dead Li were formed (Fig. 5*G*). As a comparison, the Li metal anode in the PIA-based cell has a smoother surface (Fig. 5*I*), where each Li deposit is closely contacted (Fig. 5*J*). The cross-sectional SEM image further reveals the dendrite and dead Li on the PP-reacting interface (Fig. 5*H*). More importantly, the contact interface between Li metal and the PIA separator remained intact after cycling (Fig. 5*K*), indicating the effective regulation of the PIA-derived N1–N2 synergy on Li nucleation/deposition. Besides, the cross-section of the cycled Li metal was still dense and flat after peeling off the PIA separator (Fig. 5 *K*, *Inset*).

To further visualize and compare the Li deposition morphology in the cells using PP and PIA separators, in situ optical microscopy was employed at a current density of 5.0 mA cm^{-2}. As shown in *SI Appendix,* Fig. S31, many random Li dendrites were generated on the Li metal surface in the PP separator system after 3 min deposition. Due to the inhomogeneous Li depositions, numerous dendrites are formed during the following process. By contrast, the cell using a PIA separator only shows weak Li dendrite formation throughout the deposition process. These results confirm that the PIA separator can restrict the dendrite growth and sustain a stable Li metal surface, so that the dendrite-induced electrolyte consumption, dead Li formation, and deterioration of electrode structure can be suppressed together during the LMBs cycles.

Electrochemical Performance Evaluation of the Full-Cells. The full-cells were used to evaluate the real-world application of the PIA separator. Fig. 6*A* presents the cycling stability of the LFP||Li metal full-cells using PIA and PP separator. The former shows that an initial capacity of 133 mAh g^{-1} at 1.0 C and a reversible capacity of 86.1 mAh g^{-1} after 200 cycles can be attained. However, the PP-based cell experiences a quick capacity decay (starting from 129.5 mAh g^{-1} to only 37.5 mAh g^{-1}). In addition, the comparison in the long-term cycling of the $LiNi_{0.8}Co_{0.1}Mn_{0.1}O_2$ (NCM811)||Li metal full-cells also emphasizes the effective regulation of PIA on Li deposition, as proved by the improved capacity retention of the PIA-based cell (84%) after 150 cycles (Fig. 6*C*).

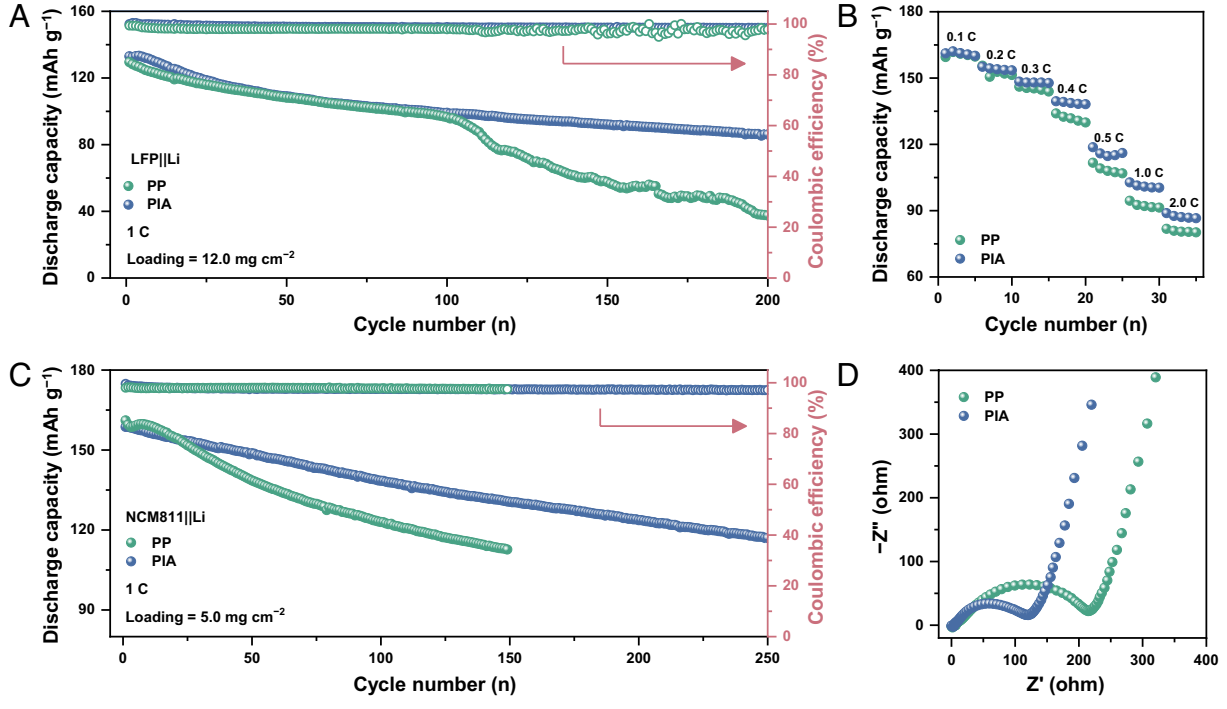

Fig. 6. Electrochemical performances of the full-cells. (*A*) Cycling performance of LFP||Li full-cells with PP and PIA separators at 1.0 C (the mass loading of LFP is 12.0 mg cm^{-2}). (*B*) Rate performance of LFP||Li full-cells with different separators. (*C*) Cycling performance of NCM811||Li full-cells with different separators at 1.0 C (the mass loading of NCM811 is 5.0 mg cm^{-2}). (*D*) Nyquist plots of LFP||Li full-cells with PP and PIA separators.

The rate performance of the LFP||Li full-cells was further determined in Fig. 6*B*. Comparing with the cell using a PP separator, the PIA-based cell delivers a higher discharge capacity of 161.2, 155.1 148.4, 139.5, 118.7, and 102.8 mAh g^{-1} at 0.1, 0.2, 0.3, 0.4, 0.5 C, and 1.0 C, respectively. Even at 2.0 C, the discharge capacity of this cell still retains at 88.9 mAh g^{-1}, while that for the PP-based cell is merely 80.9 mAh g^{-1}. It is mainly due to the lower interface resistance of the full-cell using the PIA separator (Fig. 6*D*), which endows the LMBs to provide more reversible Li^+ capacity within a fixed voltage window (*SI Appendix*, Fig. S32). Furthermore, the sustaining impedance of the full-cell using a PIA separator indicates a stable PIA/Li metal interface even after 200 cycles. However, for PP, the accumulation of dead Li on the PP/Li metal interface greatly restricts the Li^+ diffusion and migration (*SI Appendix*, Fig. S33), increasing impedance and cell failure. We also compared the PIA separator with some related ones and found that when a similar electrolyte is used, the LMBs with PIA exhibit high competitiveness in rate and operation lifetime (*SI Appendix*, Figs. S34 and S35 and Table S1). In short, this self-supporting PIA separator having the function of accelerating interfacial Li^+ diffusion and thus uniform Li nucleation can be regarded to meet the current requirement of LMBs in the field of separator engineering.

Discussion

In this contribution, we developed a self-supporting PIA separator containing rich hierarchical pores and N1–N2 synergy to regulate the interfacial Li^+ chemical behavior, for restricting the dendrite growth of Li metal. Due to the subjective N functional design, the N1 and N2 sites in the PIA separator show differences in ECD distribution. Under the electrostatic interactions, therefore, the N1 and N2 sites can "pull" and "push" the Li^+ adsorbed on the Li metal surface, respectively. This N1–N2 synergy effectively reduces the interfacial Li^+ diffusion barrier and facilitates uniform 2D Li nucleation. Besides, the PIA separator with hierarchical nanochannels also has the merits of high electrolyte wettability, high ionic conductivity, and homogeneous Li^+ flux. As a result, the PIA separator restricts the formation of local current density and dendrite growth during cycling and improves the rate performance of the LMBs. Compared with the PP separator, the Li||Cu half-cell using the PIA separator exhibits a higher reversibility of Li plating/stripping behavior in RCE, delivering an average CE (91%) over 80 cycles. Furthermore, the PIA-based full-cells consisting of LFP or NCM811 cathode both show stable long-term cycling performance with high capacity retention. Designing a separator based on the synergy from the ECD distribution opens new routes to address the challenges of LMBs.

Materials and Methods

Materials. All reagents were commercially available and used as supplied without further purification. Deuterated solvents were purchased from Cambridge Isotope Laboratory (Andover, MA). 1,3,5-tris(p-formylphenyl)benzene (TFPB) was prepared according to the established method (41). Carbonate electrolyte [1.0 M $LiPF_6$ dissolved in EC: DMC (1:1 by volume)] was purchased from the DoDoChem Co., Ltd. $LiFePO_4$ (LFP) particles, $LiNi_{0.8}Co_{0.1}Mn_{0.1}O_2$ (NCM811) particles, Super-P conductive additives (SP) and Polyvinylidene fluoride binder (PVDF) were all supplied by Guangdong Canrd New Energy Technology Co., Ltd. Li foils with a thickness of 450 μm were obtained from China Energy Lithium Co., Ltd. 1-methyl-2-pyrrolidinone (NMP) was supplied by Sigma-Aldrich.

Characterization. NMR spectra were recorded with a Bruker Avance DMX 400 spectrophotometer using of the deuterated solvent as the lock and the residual solvent or TMS as the internal reference. ^1H NMR chemical shifts are reported relative to residual solvent signals. The surface and cross-sectional and corresponding energy dispersive X-ray spectroscopy (EDX) mappings of samples were characterized employing SEM (Tescan Mira 3 XH) equipped with an Aztec X-MaxN 80. Before SEM analysis, the samples were sputter-coated with gold using an ion sputtering coating instrument (Q150T ES PLUS). The N_2 adsorption and desorption isotherms were obtained at 77 K using an automatic surface area analyzer (ASAP2460). Fourier transform infrared (FT-IR) spectroscopy was acquired on a Thermoscientific Nicolet 6700 FT-IR spectrometer at room temperature through 32 scans with a spectral resolution of 4 cm^{-1} over the range of 550 to 4,000 cm^{-1}. The thermal stability analysis was conducted using a TA Instruments Q500 thermogravimetric analyzer (TGA) under the nitrogen. Each sample (~5 mg) was heated from 50 to 800 °C with a rate of 20 °C min^{-1}. The wettability test was performed on a contact angle measuring equipment (Kino) at room temperature. Atomic force microscope (AFM) nanomechanical mapping measurements were performed in a PeakForce QNM (Quantitative Nano-Mechanics) mode on a Bruker Bio-Fast Scan AFM at ambient conditions. X-ray photoelectron spectroscopy (XPS, Nexsa) was investigated to characterize the PIA separator before and after cycling.

Electrochemical Measurement. Electrochemical tests were carried out employing CR2032-type coin cells with PP or PIA separators. All cells were assembled in an Ar-filled glove box (O_2 < 0.01 ppm, H_2O < 0.01 ppm). For full-cell: the NCM811 cathode (mass loading: 4 mg cm^{-2}) was prepared by the blade-coating method using NMP as the solvent and contains 95 wt.% NCM811 particles, 5 wt.% acetylene black, and 5 wt.% PVDF binder. The LFP cathodes (mass loading: 12 mg cm^{-2}) were fabricated using NMP as the solvent and contained 80 wt.% LFP powder, 10 wt.% acetylene black, and 10 wt.% PVDF binder. Electrolyte addition for each coin cell was 60 μL. The Li foil with a thickness of 50 μm is used as the counter electrode. The galvanostatic charge/discharge tests were performed in the potential range from 2.5 V to 3.8 V for LFP||Li full-cells (N/P = 5), and 3.0 V to 4.3 V for NCM811||Li full-cells (N/P = 12.5). All the above charge/discharge process was carried out on a Neware battery test system (CT-4008, Shenzhen, China) at ambient temperature. Cyclic voltammetry (CV) tests of LFP||Li full-cells were performed in the voltage range of 2.8 ~ 4.5 V at different scan rates. Electrochemical impedance spectra (EIS) of cells were obtained employing a frequency range from 10^6 to 10^{-1} Hz.

COMSOL Multiphysics Simulation. COMSOL Multiphysics software was used to simulate the electric field distribution and Li^+ flux at the electrode-electrolyte interface. The simulation used the Butler–Volmer expression to describe the reaction kinetics of all electrodes and the flux of each ion was calculated by the Nernst–Planck formulation. In the simplified 2D model cell, the length and width are set to 10 and 8 μm, respectively. The initial Li^+ concentration was set to 2,500 mol m^{-3}. The lower boundary of the model was set as the ground (0 V). The electrical potential of the electrode–electrolyte interface was set to 0.5 V (42). The charging current density is 0.5 C.

Density Functional Theory Calculations. The spin-polarized calculations on account of density functional theory (DFT) were determined via the DMol3 package (43). The Brillouin zones were sampled by employing the Monkhorst–Pack scheme with a 1 × 1 × 1 k-point grid and the double numerical basis sets plus the polarization functional (DNP) were used. The generalized gradient approximation (GGA) in the Perdew–Burke–Ernzerhof form and the Semicore Pseudopotential method (DSPP) with the double numerical basis sets plus the polarization functional (DNP) were used (44, 45). A DFT-D correction with the Grimme scheme was adopted to account for the dispersion interaction (46). The spin calculations were performed in the framework of the DFT with the projector augmented plane-wave method, as implemented in the Vienna ab initio simulation package (VASP) (47, 48). The generalized gradient approximation proposed by Perdew, Burke, and Ernzerhof was selected for the exchange-correlation potential (GGA-PBE) (45, 49).

Data, Materials, and Software Availability. All study data are included in the article and/or *SI Appendix*.

ACKNOWLEDGMENTS. This work was supported by the National Natural Science Foundation of China (NSFC) under Grant No. 52102282, 22071152, 22201177 and 22122105, the Fundamental Research Funds for the Central Universities (22X010201631 and 23X010301599), the Starry Night Science Fund of Zhejiang University Shanghai Institute for Advanced Study (SN-ZJU-SIAS-006), the Natural Science Foundation of Shanghai (22dz1207603 and 20ZR1429200), the Young Elite Scientists Sponsorship Program by CAST (2020QNRC001), the start-up funds from Shanghai Jiao Tong University, and the China Postdoctoral Science Foundation (2021M692061).

1. A. Banerjee *et al.*, Interfaces and interphases in all-solid-state batteries with inorganic solid electrolytes. *Chem. Rev.* **120**, 6878–6933 (2020).
2. J. Zheng *et al.*, Regulating electrodeposition morphology of lithium: Towards commercially relevant secondary Li metal batteries. *Chem. Soc. Rev.* **49**, 2701 (2020).
3. D. Lin, Y. Liu, Y. Cui, Reviving the lithium metal anode for high-energy batteries. *Nat. Nanotechnol.* **12**, 194–206 (2017).
4. C. Jin *et al.*, Rejuvenating dead lithium supply in lithium metal anodes by iodine redox. *Nat. Energy* **6**, 378–387 (2021).
5. S. Ko *et al.*, Electrode potential influences the reversibility of lithium-metal anodes. *Nat. Energy* **7**, 1217–1224 (2022).
6. K. L. Jungjohann *et al.*, Cryogenic laser ablation reveals short-circuit mechanism in Lithium Metal Batteries. *ACS Energy Lett.* **6**, 2138–2144 (2021).
7. S. Yao *et al.*, A dual-functional cationic covalent organic frameworks modified separator for high energy lithium metal batteries. *Adv. Funct. Mater.* **33**, 2212466 (2023).
8. S. Zheng *et al.*, Precise control of Li^+ directed transport via electronegative polymer brushes on polyolefin separators for dendrite-free lithium deposition. *Adv. Funct. Mater.* **32**, 2201430 (2022).
9. L. Tan *et al.*, Design of robust, lithiophilic, and flexible inorganic-polymer protective layer by separator engineering enables dendrite-free lithium metal batteries with $LiNi_{0.8}Mn_{0.1}Co_{0.1}O_2$ cathode. *Small* **17**, 2007717 (2021).
10. W. Ren *et al.*, Dendrite-free lithium metal battery enabled by dendritic mesoporous silica coated separator. *Adv. Funct. Mater.* **33**, 2301586 (2023).
11. Q. Wang *et al.*, Dual-scale Al_2O_3 particles coating for high-performance separator and lithium metal anode. *Energy Technol.* **8**, 1901429 (2020).
12. C.-Z. Zhao *et al.*, An ion redistributor for dendrite-free lithium metal anodes. *Sci. Adv.* **4**, eaat3446 (2018).
13. Y. Liu *et al.*, Dendrite-free lithium metal anode enabled by separator engineering via uniform loading of lithiophilic nucleation sites. *Energy Storage Mater.* **19**, 24–30 (2019).
14. H. Jiang, X. Lin, C. Wei, J. Feng, X. Tian, Scalable synthesis of nano-sized Bi for separator modifying in 5V-class lithium metal batteries and potassium ion batteries anodes. *Small* **18**, 2104264 (2022).
15. L. Tan *et al.*, LiF-rich and self-repairing interface induced by MgF_2 engineered separator enables dendrite-free lithium metal batteries. *Chem. Eng. J.* **442**, 136243 (2022).
16. J. Yan *et al.*, Realizing dendrite-free lithium deposition with a composite separator. *Nano Lett.* **20**, 3798–3807 (2020).
17. C. Li *et al.*, Two-dimensional molecular brush-functionalized porous bilayer composite separators toward ultrastable high-current density lithium metal anodes. *Nat. Commun.* **10**, 1363 (2019).
18. D. Han *et al.*, A graphene-coated thermal conductive separator to eliminate the dendrite-induced local hotspots for stable lithium cycling. *Adv. Energy Mater.* **12**, 2201190 (2022).
19. H. An *et al.*, Separator dependency on cycling stability of lithium metal batteries under practical conditions. *Energy Environ. Mater.* **6**, e12397 (2023).
20. X. Qi *et al.*, Covalent grafting interface engineering to prepare highly efficient and stable polypropylene/mesoporous SiO_2 separator for Li-ion batteries. *Appl. Surf. Sci.* **541**, 148405 (2021).
21. Y. Yang *et al.*, A self-supporting covalent organic framework separator with desolvation effect for high energy density lithium metal batteries. *ACS Energy Lett.* **7**, 885–896 (2022).
22. X. Zhang *et al.*, Stabilizing solid-state lithium metal batteries through in situ generated janus-heterarchical LiF-rich SEI in ionic liquid confined 3D MOF/polymer membranes. *Angew. Chem. Int. Ed.* **62**, e202304947 (2023).
23. X. Chi *et al.*, A highly stable and flexible zeolite electrolyte solid-state Li-air battery. *Nature* **592**, 551–572 (2021).
24. Y. Deng *et al.*, Novel thermotolerant and flexible polyimide aerogel separator achieving advanced lithium-ion batteries. *Adv. Funct. Mater.* **32**, 2106176 (2022).
25. X. Zhang *et al.*, Weldable and closed-loop recyclable monolithic dynamic covalent polymer aerogels. *Natl. Sci. Rev.* **9**, nwac012 (2022).
26. Z. Hao *et al.*, Functional separators regulating ion transport enabled by metal–organic frameworks for dendrite-free lithium metal anodes. *Adv. Funct. Mater.* **31**, 2102938 (2021).
27. Z. Chang, H. Yang, A. Pan, P. He, H. Zhou, An improved 9 micron thick separator for a 350 Wh/kg lithium metal rechargeable pouch cell. *Nat. Commun.* **13**, 6788 (2022).
28. G. Lin *et al.*, Metal-organic framework sandwiching porous super-engineering polymeric membranes as anionphilic separators for dendrite-free lithium metal batteries. *Adv. Funct. Mater.* **32**, 2207969 (2022).
29. S. Zhang *et al.*, A family of oxychloride amorphous solid electrolytes for long-cycling all-solid-state lithium batteries. *Nat. Commun.* **14**, 3780 (2023).
30. M. Zhang *et al.*, Boosting the temperature adaptability of lithium metal batteries via a moisture/acid-purified, ion-diffusion accelerated separator. *Adv. Energy Mater.* **12**, 2201390 (2022).
31. X. Duan *et al.*, Revealing the intrinsic uneven electrochemical reactions of Li metal anode in Ah-level laminated pouch cells. *Adv. Funct. Mater.* **33**, 2210669 (2023).
32. Y. Yang *et al.*, Hydrogen-bonded organic framework as superior separator with high lithium affinity C=N bond for low N/P ratio lithium metal batteries. *Nano Lett.* **23**, 5061–5069 (2023).
33. J. Wang *et al.*, Hierarchically porous silica membrane as separator for high-performance lithium-ion batteries. *Adv. Mater.* **34**, 2107957 (2022).
34. H. Cui *et al.*, High-voltage organic cathodes for zinc-ion batteries through electron cloud and solvation structure regulation. *Angew. Chem. Int. Ed.* **134**, e202203453 (2022).
35. P. Zhai *et al.*, Uniform lithium deposition assisted by single-atom doping toward high-performance lithium metal anodes. *Adv. Energy Mater.* **9**, 1804019 (2019).
36. R. Zhang *et al.*, Lithiophilic sites in doped graphene guide uniform lithium nucleation for dendrite-free lithium metal anodes. *Angew. Chem. Int. Ed.* **56**, 7764–7768 (2017).
37. H. Hao *et al.*, Review of multifunctional separators: Stabilizing the cathode and the anode for alkali (Li, Na, and K) metal−sulfur and selenium batteries. *Chem. Rev.* **122**, 8053–8125 (2022).
38. D. Li *et al.*, Inverted anode structure for long-life lithium metal batteries. *Adv. Energy Mater.* **12**, 2200584 (2022).
39. C. Yan *et al.*, Nucleation and growth mechanism of anion-derived solid electrolyte interphase in rechargeable batteries. *Angew. Chem. Int. Ed.* **60**, 8521–8525 (2021).
40. B. D. Adams, J. Zheng, X. Ren, W. Xu, J.-G. Zhang, Accurate determination of coulombic efficiency for lithium metal anodes and lithium metal batteries. *Adv. Energy Mater.* **8**, 1702097 (2018).
41. Z. Wang *et al.*, Phenanthro [9,10-d] imidazole as a new building block for blue light emitting materials. *J. Mater. Chem.* **21**, 5451–5456 (2011).
42. F. Wang *et al.*, Mitigating the interfacial concentration gradient by negatively charged quantum dots toward dendrite-free Zn anodes. *Energy Storage Mater.* **58**, 215–221 (2023).
43. B. Delley, From molecules to solids with the $DMol^3$ approach. *J. Chem. Phys.* **113**, 7756–7764 (2000).
44. B. Delley, Hardness conserving semilocal pseudopotentials. *Phys. Rev. B: Condens. Matter Mater. Phys.* **66**, 155125 (2002).
45. J. P. Perdew, K. Burke, M. Ernzerhof, Generalized gradient approximation made simple. *Phys. Rev. Lett.* **77**, 3865–3868 (1996).
46. S. Grimme, Semiempirical GGA-type density functional constructed with a long-range dispersion correction. *J. Comput. Chem.* **27**, 1787–1799 (2006).
47. G. Kresse, J. Furthmüller, Efficient iterative schemes for ab initio total-energy calculations using a plane-wave basis set. *Phys. Rev. B: Condens. Matter Mater. Phys.* **54**, 11169–11186 (1996).
48. G. Kresse, J. Furthmüller, Efficiency of ab-initio total energy calculations for metals and semiconductors using a plane-wave basis set. *Comput. Mater. Sci.* **6**, 15–50 (1996).
49. J. A. White, D. M. Bird, Implementation of gradient-corrected exchange-correlation potentials in car-parrinello total-energy calculations. *Phys. Rev. B: Condens. Matter Mater. Phys.* **50**, 4954–4957 (1994).